Title
Strong Electronic and Magnetic Coupling in M4 (M = Ni, Cu) Clusters via Direct Orbital Interactions between Low-Coordinate Metal Centers

Permalink
https://escholarship.org/uc/item/4k48w4zb

Journal
Journal of the American Chemical Society, 142(45)

ISSN
0002-7863

Authors
Chakarawet, Khetpakorn
Atanasov, Mihail
Marbey, Jonathan
et al.

Publication Date
2020-11-11

DOI
10.1021/jacs.0c08460

Peer reviewed

Strong Electronic and Magnetic Coupling in M₄ (M = Ni, Cu) Clusters via Direct Orbital Interactions Between Low-Coordinate Metal Centers

Khetpakorn Chakarawet,[†] Mihail Atanasov,[§,¶] Jonathan Marbey,[⊥] Philip C. Bunting,[†] Frank Neese,[§] Stephen Hill,[⊥] Jeffrey R. Long*[,†,‡,‖]

[†]Department of Chemistry and [‡]Department of Chemical and Biomolecular Engineering, University of California, Berkeley, Berkeley, California 94720, USA

[§]Max-Planck-Insitut für Kohlenforschung, Mülheim an der Ruhr D-45470, Germany

[¶]Institute of General and Inorganic Chemistry, Bulgarian Academy of Science, Akad. Georgi Bontchev, Street 11, 1113 Sofia, Bulgaria

[⊥]Department of Physics and National High Magnetic Field Laboratory, Florida State University, 1800 East Paul Dirac Drive, Tallahassee, Florida 32310, USA

[‖]Materials Sciences Division, Lawrence Berkeley National Laboratory, Berkeley, California 94720, USA

ABSTRACT: We present an extensive study of the tetranuclear transition metal cluster compounds $M_4(NP^tBu_3)_4$ and $[M_4(NP^tBu_3)_4][B(C_6F_5)_4]$ (M = Ni, Cu; ^tBu = *tert*-butyl), which feature low-coordinate metal centers and direct metal–metal orbital overlap. X-ray diffraction, electrochemical, magnetic, spectroscopic, and computational analysis elucidate the nature of the bonding interactions in these clusters and the impact of these interactions on the electronic and magnetic properties. Direct orbital overlap results in strongly-coupled, large-spin ground states in the clusters $[Ni_4(NP^tBu_3)_4]^{+/0}$ and fully delocalized, spin-correlated electrons. Correlated electronic structure calculations confirm the presence of ferromagnetic ground states that arise from direct exchange between magnetic orbitals, and, in the case of the neutral cluster, itinerant electron magnetism similar to that in metallic ferromagnets. The cationic nickel cluster also possesses large magnetic anisotropy, exemplified by a large, positive axial zero-field splitting parameter of $D = +7.95$ or $+9.2$ cm⁻¹, as determined by magnetometry or electron paramagnetic resonance spectroscopy, respectively. The $[Ni_4(NP^tBu_3)_4]^+$ cluster is also the first molecule with easy-plane magnetic anisotropy to exhibit zero-field slow magnetic relaxation, and, under a small applied field, it exhibits relaxation exclusively through an Orbach mechanism with a spin relaxation barrier of 16 cm⁻¹. The $S = \frac{1}{2}$ complex $[Cu_4(NP^tBu_3)_4]^+$ exhibits slow magnetic relaxation via a Raman process on the millisecond timescale, supporting the presence of slow relaxation via an Orbach process in the nickel analogue. Overall, this work highlights the unique electronic and magnetic properties that can be realized in metal clusters featuring direct metal–metal orbital interactions between low-coordinate metal centers.

Introduction

Molecular magnetism broadly encompasses the design and study of molecules and molecule-based materials exhibiting magnetic properties, and is largely motivated by prospective applications in areas such as magnetic memory, spintronics, quantum computing, and permanent magnetism.[1,2] Multinuclear transition metal complexes have attracted considerable interest in this regard, due in large part to the discovery that magnetic exchange interactions in such molecules can give rise to numerous interesting properties, particularly single-molecule magnet behavior.[3] Indeed, the field of single-molecule magnetism originated following the discovery of slow magnetic relaxation in the dodecanuclear cluster $Mn_{12}O_{12}(CH_3CO_2)_{16}(H_2O)_4$, wherein uncompensated antiferromagnetic superexchange interactions between manganese ions gives rise to a large-spin ground state.[4] Since then, many multinuclear metal clusters exhibiting single-molecule magnet behavior have been reported.[5] Most of these clusters feature metal ions coupled via weak, antiferromagnetic superexchange interactions. Recently, however, a number of clusters exhibiting strong ferromagnetic direct exchange, mediated by direct metal–metal orbital overlap, have been reported.[6–12] These complexes have motivated a new design paradigm for accessing single-molecule magnets with thermally isolated large-spin ground states.[11,12] For example, the tetranuclear iron cluster $Fe_4(N=CPh_2)_6$ was recently shown to exhibit an $S = 7$ ground state and consequently slow magnetic relaxation with a spin relaxation barrier of $U_{eff} = 29$ cm⁻¹.[12] We also recently reported the tetranuclear cluster compound $[Co_4(NP^tBu_3)_4][B(C_6F_5)_4]$,[11] which possesses a well-isolated $S = \frac{9}{2}$ ground state resulting from direct metal–metal orbital overlap. Crucially, the low-coordinate metal centers in this complex additionally give rise to a very large magnetic anisotropy, with $D = -12.34$ cm⁻¹, resulting in the largest barrier to magnetic relaxation yet characterized for any transition metal cluster, $U_{eff} = 87$ cm⁻¹.

More broadly, with the steadily growing number of metal clusters featuring direct metal–metal interactions, the possibility emerges to access unique electronic properties otherwise unattainable in traditional metal clusters, such as high levels of electron delocalization[9] and meta-atom behavior.[7] Density

functional theory has been widely used to study magnetic properties of iron–sulfur clusters featuring direct metal–metal interactions.[13,14] Nonetheless, configuration interactions have only been applied to computational studies of dinuclear complexes due in part to the challenge in the complex electronic structures of these metal clusters.[15–18] Indeed, such studies are potentially of great significance beyond the elucidation of molecular properties, as magnetic direct exchange through delocalized electrons also governs permanent magnetism in ferromagnets possessing high Curie temperatures, such as metallic iron, cobalt, and nickel.[19,20] Magnetic studies of polynuclear metal complexes[1,15,21,22] have previously enabled the refinement of an earlier model for superexchange originally proposed in solid MnO.[23] Likewise, the detailed electronic, magnetic, and theoretical investigation of paramagnetic metal clusters featuring direct metal–metal orbital overlap stands as an important area of fundamental inquiry with the potential to provide new insights into magnetic exchange in metallic clusters and bulk metals.

Here, we report the metal–metal bonded complexes $[Ni_4(NP^tBu_3)_4]^{+/0}$, which exhibit large magnetic anisotropy and large-spin ground states that are thermally persistent to 300 K. Correlated electronic structure *ab initio* calculations are employed to rationalize the effect of metal–metal interactions on the magnetic properties, and they reveal strong Ni–Ni ferromagnetic coupling arising from a direct exchange mechanism resembling that in ferromagnetic metals. The complex $[Ni_4(NP^tBu_3)_4]^+$ is also the first easy-plane molecular magnet to exhibit slow magnetic relaxation under zero applied field, while under a small applied field the complex relaxes solely through an Orbach mechanism. In addition, we synthesized the cationic $S = 1/2$ tetranuclear copper analogue $[Cu_4(NP^tBu_3)_4]^+$, which exhibits spin-vibronic relaxation on the millisecond timescale at low temperatures, suggesting that the observation of Orbach barrier in the nickel analogue is also a result of slow spin-vibronic relaxation. These findings highlight the unique electronic and magnetic properties accessible with complexes featuring metal–metal bonding interactions.

Results and Discussion

Synthesis and Characterization. The compound $Ni_4(NP^tBu_3)_4$ (**1**) was prepared via a modification of a previously reported synthesis.[24] In brief, the salt metathesis reaction of $LiNP^tBu_3$ and $NiBr_2$ in tetrahydrofuran (THF) and 1,2-dimethoxyethane was followed by *in situ* reduction with KC_8 to yield the desired product, which was separated from the reaction mixture by extraction with hexane. Compound $\mathbf{1}\cdot n\text{-}C_6H_{14}$ was isolated as dark green block-shaped crystals from a concentrated hexane solution stored at −30 °C. Single-crystal X-ray diffraction characterization revealed that $\mathbf{1}\cdot n\text{-}C_6H_{14}$ crystallizes in the space group $C2/c$, with a crystallographic two-fold rotation axis passing through two diagonal Ni atoms of the cluster, similar to the previously reported structure of $\mathbf{1}\cdot2\text{THF}$.[24] The molecule adopts an idealized D_{2d} symmetry (Figure S1). Each Ni atom is coordinated by the N atoms of two phosphinimide ligands, resulting in an almost linear coordination geometry around each Ni center, with an average N–Ni–N angle of 176.4(6)°. All Ni atoms lie within the same plane, as dictated by the crystallographic two-fold symmetry. The average of the four Ni···Ni distances is 2.3631(1) Å, which is within range of direct metal–metal interactions.[25]

Oxidation of **1** using $[FeCp_2][B(C_6F_5)_4]$ (Cp^- = cyclopentadienyl anion) yielded $[Ni_4(NP^tBu_3)_4][B(C_6F_5)_4]$ (**2**) as a dark blue
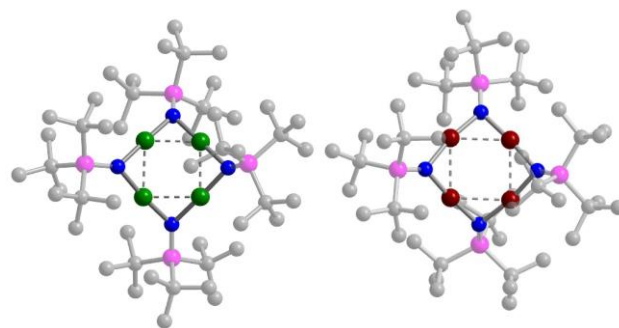
Figure 1. Crystal structures of the cationic cluster in $[Ni_4(NP^tBu_3)_4][B(C_6F_5)_4]$ (**2**) (left) and the neutral cluster $Cu_4(NP^tBu_3)_4$ (**3**) (right). Dark red, green, pink, blue, and gray spheres represent Cu, Ni, P, N, and C atoms, respectively; H atoms are omitted for clarity. Only one orientation of each disordered molecule is shown.

Table 1. Selected Average Interatomic Distances (Å) and Angles (°) for the Tetranuclear Clusters in $Ni_4(NP^tBu_3)_4$ (1), $[Ni_4(NP^tBu_3)_4][B(C_6F_5)_4]$ (2), $Cu_4(NP^tBu_3)_4$ (3), and $[Cu_4(NP^tBu_3)_4][B(C_6F_5)_4]$ (4) Determined from Single-Crystal X-ray Diffraction[a]

	1	2	3	4
M···M	2.3631(1)	2.40(4)	2.582(4)	2.53(3)
M–N	1.855(6)	1.836(6)	1.861(5)	1.84(6)
N–M–N	176.4(6)	177(2)	173(3)	169(3)

[a]The standard deviations calculated from the values of interatomic parameters are given in parentheses. The estimated standard uncertainty of each parameter is given in Table S3.

powder that could be crystallized as dark blue block-shaped crystals from a THF/hexane mixture at −30 °C. X-ray diffraction analysis revealed that the compound crystallizes in the space group $P2_12_12_1$ and that the tetranuclear cluster retains its structural integrity upon oxidation (Figure 1, left). The average Ni–N distance in **2** is shorter than in **1** (1.836(6) versus 1.855(6) Å, respectively), while the average Ni···Ni distance is longer than in **1** (2.40(4) versus 2.3631(1) Å) (Table 1). All of the Ni–N bond lengths decrease upon oxidation of **1** to **2** (Table S3); thus, it was not possible to identify a localized site of oxidation in the complex. This result is consistent with the presence of delocalized electrons in a metal–metal bonded cluster, as will be discussed in detail below.

The neutral copper compound $Cu_4(NP^tBu_3)_4$ (**3**) was synthesized via protonolysis of mesitylcopper(I) by HNP^tBu_3. Crystallization from hexane at −30 °C yielded large, colorless block-shaped crystals of $\mathbf{3}\cdot n\text{-}C_6H_{14}$ suitable for X-ray diffraction analysis, which revealed that the compound is isomorphous and isostructural to **1** (Figure 1, right). In $\mathbf{3}\cdot n\text{-}C_6H_{14}$, the average Cu···Cu distance of 2.582(4) Å is much longer than the Ni···Ni distance of 2.3631(1) Å in $\mathbf{1}\cdot n\text{-}C_6H_{14}$ (Table 1), which may be attributed to population of the extra electron from each copper in metal–metal antibonding orbitals, resulting in a total Cu···Cu bond order of zero (see below).

Oxidation of **3** by $[FeCp_2][B(C_6F_5)_4]$ yielded $\mathbf{4}\cdot1.4\text{DFB}\cdot0.3 n\text{-}C_6H_{14}$ (DFB = 1,2-difluorobenzene) as black rod-shaped crystals after recrystallization from DFB/hexane at −30 °C. Compound **4** crystallizes in the space group $P\bar{1}$, and initial structure
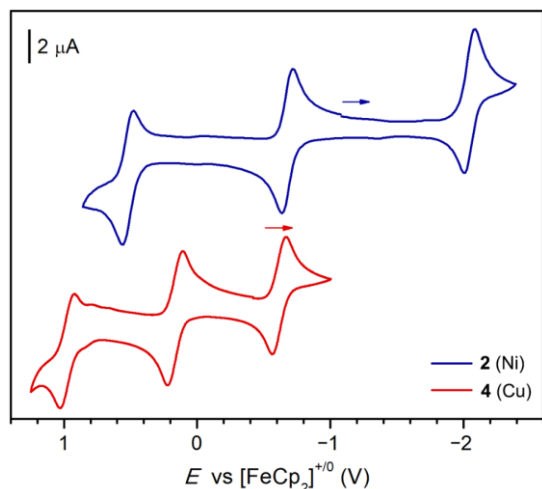
Figure 2. Cyclic voltammograms for **2** (blue) and **4** (red), obtained in DFB solution containing 1 mM analyte and 0.1 M of the electrolyte (^{n}Bu$_4$N)PF$_6$. The arrow represents the starting point and the direction of the scan.

Figure 3. Molar magnetic susceptibility times temperature ($\chi_M T$) versus T data for **1** (green), **2** (blue), and **4** (red) collected under a 1000 Oe field and over temperatures ranging from 2 to 300 K. The data for **1** and **4** were corrected for contributions from temperature-independent paramagnetism using χ_{TIP} = 1.0×10^{-3} and 9.5×10^{-4} cm^3/mol, respectively.

refinement revealed an intact tetranuclear cluster (Figure S4). In addition, two sites of residual electron density were located in the Fourier-difference map above and below the Cu$_4$ plane. Further analysis revealed that this electron density corresponds to the disordered pentanuclear copper(I) species [Cu$_5$(NP^{t}Bu$_3$)$_4$][B(C$_6$F$_5$)$_4$] (Figure S5), which was further confirmed by mass spectrometry (Figure S7). Refinement of the diffraction data for **4**·1.4DFB·0.3n-C$_6$H$_{14}$ revealed that this compound consists of 81% [Cu$_4$(NP^{t}Bu$_3$)$_4$][B(C$_6$F$_5$)$_4$] co-crystallized with 19% [Cu$_5$(NP^{t}Bu$_3$)$_4$][B(C$_6$F$_5$)$_4$]. A comparison of the metrical parameters of [Cu$_4$(NP^{t}Bu$_3$)$_4$][B(C$_6$F$_5$)$_4$] with the parent neutral compound revealed that the Cu···Cu and Cu–N distances decrease slightly in the cationic cluster (Tables 1 and S3), as expected upon the removal of an electron from an antibonding orbital (see below).

Electrochemistry. The cyclic voltammogram collected for **2** in DFB features the expected one-electron [Ni$_4$(NP^{t}Bu$_3$)$_4$]$^{+/0}$ redox couple at $E_{1/2}$ = –2.02 V versus [FeCp$_2$]$^{+/0}$ (Figure 2). Two additional one-electron processes occur at $E_{1/2}$ = –0.66 and +0.54 V, corresponding to the [Ni$_4$(NP^{t}Bu$_3$)$_4$]$^{2+/+}$ and [Ni$_4$(NP^{t}Bu$_3$)$_4$]$^{3+/2+}$ redox couples, respectively. Comproportionation constants of 1.0 × 10^{23} and 2.1 × 10^{20} were determined for the mixed-valence complexes [Ni$_4$(NP^{t}Bu$_3$)$_4$]$^+$ and [Ni$_4$(NP^{t}Bu$_3$)$_4$]$^{2+}$, respectively. These values are much larger than those of typical mixed-valence complexes, and are indicative of a delocalized electronic structure arising from direct metal–metal orbital overlap.[7,10,11]

The cyclic voltammogram for **4** in DFB features three one-electron processes at –0.63, +0.17, and +0.98 V, assigned to the [Cu$_4$(NP^{t}Bu$_3$)$_4$]$^{+/0}$, [Cu$_4$(NP^{t}Bu$_3$)$_4$]$^{2+/+}$, and [Cu$_4$(NP^{t}Bu$_3$)$_4$]$^{3+/2+}$ couples, respectively (Figure 2). Comproportionation constants of 1.9 × 10^{13} and 5.0 × 10^{13} were determined for the mixed-valence complexes [Cu$_4$(NP^{t}Bu$_3$)$_4$]$^+$ and [Cu$_4$(NP^{t}Bu$_3$)$_4$]$^{2+}$, respectively. These values are several orders of magnitude smaller than those determined for the Ni analogues, possibly because of the longer M···M distances. Nonetheless, the values are still large among mixed-valence complexes, and both systems are best described as possessing electrons that are delocalized over molecular orbitals formed by direct metal orbital overlap.
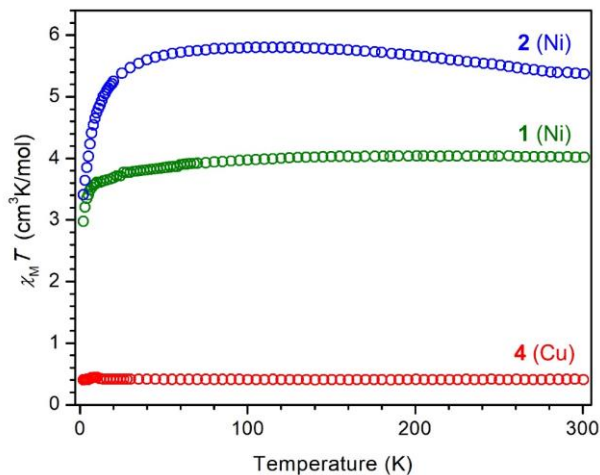
Static Magnetic Measurements. Variable-temperature dc magnetic susceptibility data were collected for crystalline samples of **1**·n-C$_6$H$_{14}$, **2**, and **4**·1.4DFB·0.3n-C$_6$H$_{14}$ under an applied dc field of 1000 Oe (Figure 3). The susceptibility data for **1** and **4** were corrected for contributions from temperature-independent paramagnetism (χ_{TIP} ~ 10^{-3} cm^3/mol), and the data for **4** were additionally corrected to remove the diamagnetic contribution from the minor impurity [Cu$_5$(NP^{t}Bu$_3$)$_4$][B(C$_6$F$_5$)$_4$]. The value of $\chi_M T$ at 300 K for [Cu$_4$(NP^{t}Bu$_3$)$_4$][B(C$_6$F$_5$)$_4$] in **4** is 0.498 cm^{3}K/mol, consistent with an S = $^1/_2$ system (g_{iso} = 2.30). In contrast, the $\chi_M T$ product for **1** at 300 K is 4.02 cm^{3}K/mol, which is much higher than the predicted value of 1.50 cm^{3}K/mol for four isolated S = $^1/_2$ nickel (I) centers. Instead, the experimental value better corresponds to an S = 2 ground state with g_{iso} = 2.32. The room temperature $\chi_M T$ product for **2** is 5.37 cm^{3}K/mol, best corresponding to an S = $^5/_2$ ground state (predicted $\chi_M T$ = 4.375 cm^{3}K/mol for g = 2). The presence of such large-spin ground states in **1** and **2** at 300 K is indicative of strongly correlated electron spins mediated by direct metal–metal orbital overlap.[7,10,11]

With decreasing temperature, $\chi_M T$ for **2** increases initially to a value of 5.80 cm^{3}K/mol at 130 K, similar to what has been previously observed in other metal–metal bonded systems.[10,26] This increase is attributed to the depopulation of a low-lying S = $^3/_2$ excited state with smaller magnetic moment (see below). A fit of the magnetic susceptibility data from 150 to 300 K using the van Vleck equation and assuming an S = $^5/_2$ ground state and S = $^3/_2$ excited state yielded an energy separation of 221 cm^{-1} (Figure S8). Below ~90 K, $\chi_M T$ gradually decreases until a dramatic downturn at ~40 K, reaching a value of 3.41 cm^{3}K/mol at 2 K. In contrast, $\chi_M T$ for **1** exhibits much less variation across the examined temperature range. In particular, the data uniformly and gradually decrease from 300 to ~20 K before dropping to a value of 3.00 cm^{3}K/mol at 2 K. The low-temperature drop in the data for compounds **1** and **2** is indicative of significant zero-field splitting.

Low-temperature magnetization measurements were carried out to further quantify magnetic anisotropy in **1** and **2** and the

tetranuclear cluster in **4**. For compound **4**, the reduced magnetization plot features superimposable isofield lines, as expected for an $S = \frac{1}{2}$ spin system (Figure S9). In contrast, the reduced magnetization plots for **1** and **2** feature non-superimposable isofield lines (Figures S10 and S11), indicative of significant zero-field splitting. The magnetization data for **1** and **2** were accordingly fit using the following Hamiltonian:

$$\hat{H} = D\hat{S}_z^2 + E(\hat{S}_x^2 - \hat{S}_y^2) + \mu_B H \cdot g \cdot S \qquad (1)$$

where D and E are the axial and transverse zero-field splitting parameters, respectively, $S_{x/y/z}$ is the electron spin projection operator onto the $x/y/z$ axis, μ_B is the Bohr magneton, g is the Landé g-tensor, and H is the magnetic field. The fits yielded parameters of $D = -1.93(1)$ cm^{-1}, $|E| = 0.53(3)$ cm^{-1}, $g_\parallel = 2.180(2)$, and $g_\perp = 2.249(1)$ for **1**, and $D = +7.95(5)$ cm^{-1}, $E = 1.17(1)$ cm^{-1}, $g_\parallel = 2.28(1)$, and $g_\perp = 2.188(1)$ for **2**.

It is important to note that the vast majority of transition metal clusters exhibit $|D| < 1$ cm^{-1},[5] for example $D = -0.46$ cm^{-1} for Mn$_{12}$O$_{12}$(O$_2$CCH$_3$)$_{16}$(OH$_2$)$_4$ ($S = 10$),[27] although smaller spin clusters may exhibit slightly larger $|D|$ values. For instance, the $S = 3$ compound [Ni$_3$L$_3$(OH)(Cl)](ClO$_4$) (HL = 2-[(3-dimethyl-aminopropylimino)methyl]phenol) exhibits a value of $D = -1.32$ cm^{-1}, previously record among Ni clusters.[28] The even larger D values measured for **1** and **2** likely arise from the weak ligand field generated by the formally two-coordinate environment, as demonstrated previously for [Co$_4$(NP^{t}Bu$_3$)$_4$][B(C$_6$F$_5$)$_4$].[11] Indeed, a low-coordinate environment is ideal for generating large anisotropy,[29] because the associated weak ligand field minimizes the energy splitting between states contributing to orbital angular momentum, thus maximizing zero-field splitting generated through second-order spin-orbit coupling.

Electron Paramagnetic Resonance. High-field, high-frequency EPR spectra were collected to more accurately quantify the magnetic anisotropy in Ni$_4$(NP^{t}Bu$_3$)$_4$ (**1**) and [Ni$_4$(NP^{t}Bu$_3$)$_4$][B(C$_6$F$_5$)$_4$] (**2**). Data were collected on crystalline powder samples using microwave frequencies in the range of 60–532 GHz and magnetic fields between 0 and 14.5 T.[30] Representative spectra shown in Figure 4 are markedly different for the two compounds. The spectra for **1** exhibit multiple sharp transitions between 64 and 512 GHz (Figure S12a), while the spectra for **2** obtained at frequencies between 65 and 224 GHz are characterized by two broad intra-Kramers transitions that correspond to field orientations along the principal components (z and xy) of the zero-field splitting tensor (Figure S14). Both sets of spectra could be accurately simulated from the parameterization provided by the spin Hamiltonian in Equation 1, using the EasySpin toolbox in Matlab.[33] A brief summary of the procedures used to determine the zero-field splitting parameters for **1** and **2** from the EPR data is as follows. For **1**, the temperature dependence of the EPR spectra at 406 GHz was examined in order to identify the ground state-based EPR transition (Figure S13a, red label). A linear fit of frequency versus field for this transition (Figure S12b) was extrapolated to obtain a zero-field frequency of 154(2) GHz, corresponding to a value of $D = -1.74$ cm^{-1} associated with the ground $M_S = -2$ state to the excited $M_S = -1$ state transition, with an isotropic g-value of $g_{iso} = 2.2$. The experimental data were simulated using $D = -1.74$ cm^{-1} and a rhombic zero-field splitting term of $|E| = 0.24$ cm^{-1}, which was necessary to replicate the splitting between the x and y components of the spectra (Figure 4, upper, red traces). These zero-field splitting parameters are in good agreement with those obtained from fits of the magnetization data.
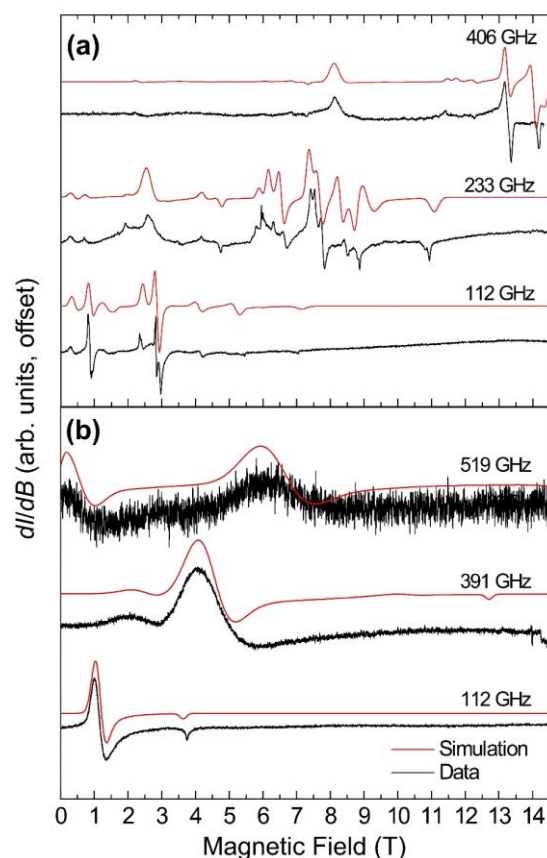

Figure 4. Multi-frequency powder EPR spectra for **1** (upper) and **2** (lower), with simulations shown as red traces. All data were collected at 5 K to ensure each sample was close to the maximum population of its spin-projected M_S ground state.

Between 65 and 224 GHz, the EPR spectra for **2** feature only two transitions corresponding to the $M_S = \pm\frac{1}{2}$ Kramers doublet (Figure S14). However, at the highest examined frequencies, another transition is clearly present near zero field (Figure 4, lower, and Figure S15a). The temperature dependence of spectra collected at 486 GHz (Figure S15b) revealed that this resonance position corresponds to the transition from the ground $M_S = -\frac{1}{2}$ to the $M_S = -\frac{3}{2}$ excited state, thus affording direct spectroscopic evidence of zero-field splitting in **2**. The EPR spectra of **2** were well-simulated with $D = +9.2$ cm^{-1}, $E = 0$, $g_\perp = 2.4$ and $g_\parallel = 2.2$, for an $S = \frac{5}{2}$ spin system (Figure 4, lower, red), in agreement with the results from magnetization measurements.

Finally, the X-band EPR spectrum for **4** collected at 2 K in frozen 2-methyltetrahydrofuran (2-MeTHF) features a very broad signal centered around $g = 2.07$ (Figure S16). The broad spectrum is presumed to result from extensive hyperfine interactions involving the four Cu nuclei (^{63}Cu and ^{65}Cu isotopes, both with $I = \frac{3}{2}$), ligand disorder, and paramagnetic relaxation.

Electronic Structure Analysis. Thermally-persistent, large-spin ground states in clusters with direct metal–metal interactions have been rationalized as arising from electrons in molecular orbitals generated from direct orbital overlap.[6,7,9–11,16,17] However, detailed calculations to support this hypothesis have only been performed on dinuclear complexes.[16,17] Here, a qualitative molecular orbital analysis (Figure 5) was performed in
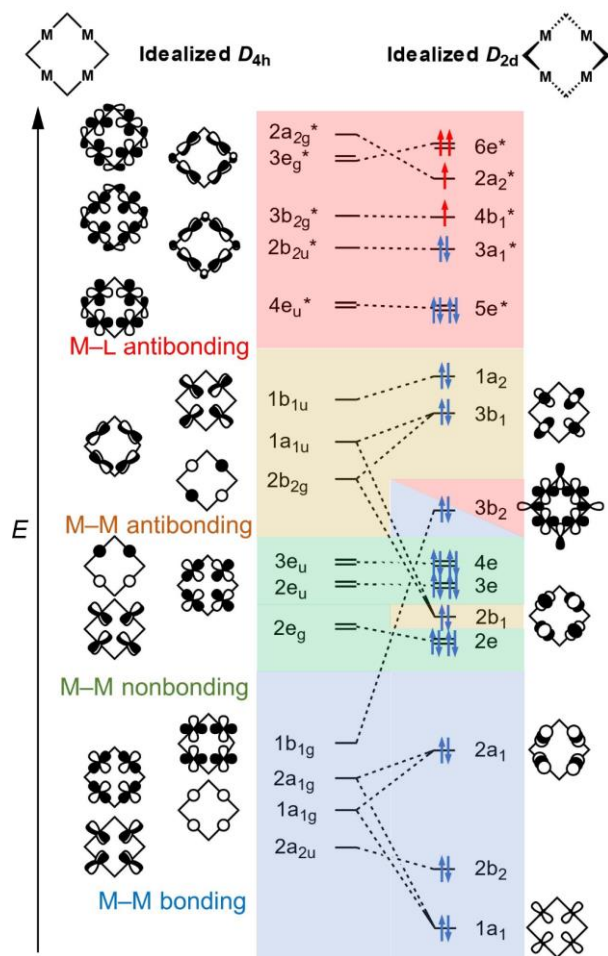
Figure 5. Molecular orbital energy level diagrams for a hypothetical square $Ni_4(NPR_3)_4$ cluster with D_{4h} symmetry (left) and $Ni_4(NP^tBu_3)_4$ cluster (**1**) with D_{2d} symmetry (right). The positions and orbital interactions on the right were corroborated by DFT calculations (see Figures S17 and S18). Orbitals dominated by metal–ligand antibonding, metal–metal antibonding, metal–metal nonbonding, and metal–metal bonding interactions are shaded in red, yellow, green, and blue, respectively. Blue and red arrows represent paired and unpaired electrons, respectively. Calculated orbital energy levels for **1** are provided in Figure S18. This diagram can also apply to a $Cu_4(NP^tBu_3)_4$ cluster in **3** by adding four more valence electrons.

tandem with density functional theory (DFT) calculations (Figures S17 and S18) to better understand the nature of the orbital interactions within the $Ni_4(NP^tBu_3)_4$ cluster and the associated magnetic behavior.

A molecular orbital diagram was first constructed for a hypothetical planar molecule in D_{4h} symmetry as shown on the left side of Figure 5. Here, 20 metal 3d orbitals may engage in bonding interactions according to symmetry considerations. Seven metal group orbitals interact with the 2p group orbitals of the coordinated N atoms, resulting in seven M–L antibonding orbitals (Figure 5 left, red). The remaining 13 orbitals are metal-centered, and form four M–M bonding, six M–M nonbonding, and three M–M antibonding molecular orbitals (Figure 5, left; blue, green, and yellow, respectively). Upon lowering the molecular symmetry from D_{4h} to idealized D_{2d} symmetry, the $1b_{1g}$ M–M bonding orbital mixes with a ligand group orbital to form

a $3b_2$ orbital (Figure 5, right), as also indicated by DFT calculations (Figure S17). Furthermore, a Walsh analysis reveals that M–L and M–M interactions are of approximately the same order of magnitude, which is the result of the weak ligand field originating from the two-coordinate metal environment. The overall 3d orbital energy splitting determined from DFT calculations is 25,000 cm^{-1} (Figure S18).

According to the molecular orbital diagram for idealized D_{2d} symmetry, oxidation of $Ni_4(NP^tBu_3)_4$ to $[Ni_4(NP^tBu_3)_4]^+$ is associated with the removal of an electron from the $3a_1^*$ orbital, which has partial metal–metal bonding character (Figure S19, upper). Loss of this electron results in a lengthening of the Ni$\cdots$Ni distance, as shown by X-ray diffraction analysis (Table 1). In contrast, oxidation of $Cu_4(NP^tBu_3)_4$ to $[Cu_4(NP^tBu_3)_4]^+$ results in the removal of an electron from the $6e^*$ orbital, which has partial M–M antibonding character (Figure S19, lower). This change results in a shortening of the Cu$\cdots$Cu distances, as observed in a comparison of the solid-state structures of both compounds. It should be noted that, based on this analysis, $Cu_4(NP^tBu_3)_4$ has a total M–M bond order of zero, which is reflected in its longer M$\cdots$M distance compared to the M_4 clusters in **1**, **2**, and **4**. In both $Ni_4(NP^tBu_3)_4$ and $Cu_4(NP^tBu_3)_4$, oxidation leads to shortening of the M–N distances (Table 1), as expected for the removal of an electron from a M–L antibonding orbital.

The spin energy levels of the truncated model complexes $Ni_4(NPH_3)_4$ (**1′**) and $[Ni_4(NPH_3)_4]^+$ (**2′**) were computed using the complete active space self-consistent field (CASSCF) method[31] modulated by second order N-electron valence perturbation theory (NEVPT2),[32–34] as implemented in the program ORCA.[35] Calculations on **1′** were carried out by correlating four electrons on four localized 3d molecular orbitals [CAS(4,4)] and extended active spaces, correlating twelve electrons on eight [CAS(12,8)] and twenty eight electrons on sixteen [CAS(28,16)] localized molecular orbitals. All of these calculations yielded a well-isolated $S = 2$ ground state (Table S5). From the CASSCF calculation, an electron-transfer energy of 6.1 eV was found between the lateral pairs of Ni centers, indicating a dominant exchange pathway through adjacent metal centers (Figure 6). Moreover, a calculation with an extended active space, which included the lower-lying, fully occupied orbitals, revealed excited states resulting in two unpaired electrons on a Ni^{2+} site in **1′**, for which parallel spin alignment is governed by
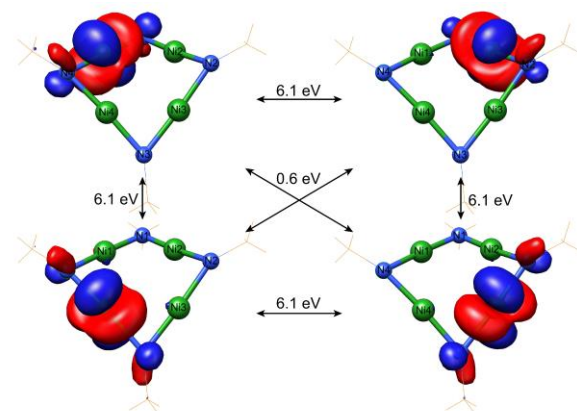

Figure 6. Localized magnetic orbitals for **1′**, as obtained from CAS(4,4) calculations with computed charge transfer parameters between the lateral (6.1 eV) and diagonal (0.6 eV) Ni–Ni pairs. Green and blue spheres represent Ni and N atoms, respectively.
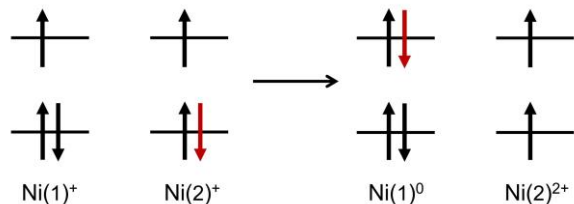
Figure 7. Schematic illustration of the excited states in **1′** (right) found from CASSCF calculations using an extended active space. The excited state features a Ni^{2+} center with parallel alignment of spins according to Hund's rule. The itinerant electron is highlighted in red.

Hund's rule (Figure 7). This interaction further stabilizes the $S = 2$ ground state such that the $S = 0$ excited state is ~1000 cm^{-1} higher in energy (with CAS(28,16) active space, Table S5). The observed excitation is reminiscent of ferromagnetism in magnetic metals, where a broad s conduction band overlaps with half-filled narrow d band, providing a pathway for direct exchange via itinerant electrons, where the ferromagnetic exchange interaction is governed by Hund's rule on each metal atom.[20]

Calculations performed on **2′** confirmed an $S = \frac{5}{2}$ ground state and the presence of an $S = \frac{3}{2}$ excited state that lies 73 cm^{-1} higher in energy (Table S6). This value is smaller than the ground to first excited state splitting determined from fitting the $\chi_M T$ versus T data for **2** from 150 to 300 K using the van Vleck equation (221 cm^{-1}, see Figure S8). However, in both cases the separation is such that population of $S = \frac{3}{2}$ excited state is expected at ambient temperature according to Boltzmann statistics, consistent with the temperature dependence of the $\chi_M T$ data for **2** (Figure 3).

Magnetization Relaxation Dynamics. Systems exhibiting large negative values of D (easy-axis anisotropy) were long the primary focus in the pursuit of new single-molecule magnets for two main reasons: $D < 0$ gives rise to a maximal $\pm M_S$ ground state and the suppression of quantum tunneling of the magnetization, and for integer S, only systems with $D < 0$ are guaranteed to exhibit the doubly degenerate ground state required for slow magnetic relaxation.[3] However, in recent years a number of molecules with easy-plane anisotropy $D > 0$ and half-integer spins have been found to show slow magnetic relaxation under an applied field.[36,37] Spin inversion within the ground state in such systems is prohibited by Kramers theorem, and thus slow magnetic relaxation occurs via Orbach, Raman, and/or hyperfine-interaction-mediated direct processes.[38] Given the presence of a significant easy-plane anisotropy in **2**, it was therefore of interest to probe the dynamic magnetic properties of this compound.

Ac magnetic susceptibility measurements were first carried out on a crystalline sample of **2**. Under zero applied field, compound **2** exhibits no signal in the molar out-of-phase susceptibility (χ_M''). However, under a small applied field of 400 Oe, peaks in χ_M'' were observed between 1.80 and 2.05 K (Figure S21). Relaxation times (τ) were extracted from these data using a generalized Debye model,[3] and a corresponding plot of the logarithm of τ vs inverse T is linear (Figure S29), suggesting that the magnetization relaxes via an Orbach process. The temperature-dependent relaxation data were fit using the equation:

$$\tau^{-1} = \tau_0^{-1}\exp\left(-\frac{U_{\text{eff}}}{k_B T}\right) \qquad (2)$$

to yield an effective spin reversal barrier $U_{\text{eff}} = 16.53(6)$ cm^{-1} and pre-exponential factor $\tau_0 = 4.7(2) \times 10^{-10}$ s. The value of U_{eff} is in good agreement with the first magnetic excited states calculated from high-field EPR and magnetization data (18 and 19 cm^{-1}, respectively), while the value of τ_0 is in the range expected for an Orbach relaxation process.[3] Accordingly, Orbach relaxation in **2** occurs via the first excited $M_S = \pm\frac{3}{2}$ states. It should be noted that other relaxation processes, such as quantum tunneling of magnetization and Raman relaxation, appear to be completely suppressed in the narrow temperature range studied, in contrast to other single-molecule magnets with easy-plane anisotropy.[37]

The absence of slow magnetic relaxation in **2** under zero field could be attributed to fast quantum tunneling resulting from dipolar interactions or intramolecular hyperfine interactions. To investigate the relevance of dipolar interactions, ac susceptibility data were collected on a dilute (10 mM) frozen solution of **2** in 2-MeTHF. Significantly, zero-field slow magnetic relaxation is clearly visible at high frequencies for this sample (Figure S23). This observation indicates that intermolecular interactions are at least partially responsible for fast relaxation under zero field in the crystalline sample, and intramolecular quantum tunneling of magnetization appears to be relatively slow in this cluster. Moreover, after applying 0.3 T field and subsequent removal of the magnetic field, temperature-dependent zero-field relaxation is visible (Figure S25), presumably because random dipole moments are reoriented. Relaxation times can be fit solely to an Orbach process with $U_{\text{eff}} = 16.0(4)$ cm^{-1} and $\tau_0 = 7.9(22) \times 10^{-9}$ s (Figure S29), although not all molecules relax at this rate as indicated by a relatively large adiabatic susceptibility (Table S7). To the best of our knowledge, **2** is the first compound with easy-plane anisotropy to exhibit slow magnetic relaxation under zero field, a consequence of its Kramers degeneracy, large magnetic anisotropy, and low abundance of isotopes with nuclear spin (~1% natural abundance of ^{61}Ni). It is noteworthy that zero-field relaxation has been predicted for Kramers ions with $D > 0$ and no nuclear spin,[38] but has not previously been realized due to the lack of systems with appropriate electronic structures. For example, in the case of a mononuclear nickel system, high-spin nickel(III) would be required to access an electronic structure suitable for zero field slow magnetic relaxation.[38] However, the low-coordinate nickel centers engaged in direct metal–metal orbital overlap in **2** give rise to a unique electronic structure that facilitates slow magnetic relaxation in a more synthetically accessible system. Finally, application of a small optimal field of 200 Oe further suppresses fast spin relaxation, enabling coherent relaxation observed in the out-of-phase susceptibility between 1.8 and 2.1 K (Figure S27). An Arrhenius plot of the corresponding relaxation times versus inverse T were again fit to an Orbach process, yielding $U_{\text{eff}} = 15.7(2)$ cm^{-1} and $\tau_0 = 1.4(2) \times 10^{-9}$ s (Figures 8 and S29).

Although compound **1** possesses easy-axis anisotropy (with D values of –1.93 and –1.74 cm^{-1} determined from magnetization and EPR data, respectively), it does not exhibit any signatures of slow magnetic relaxation at temperatures as low as 2 K and ac frequencies as high as 1500 Hz. This absence is likely due to the small ground state to first magnetic excited
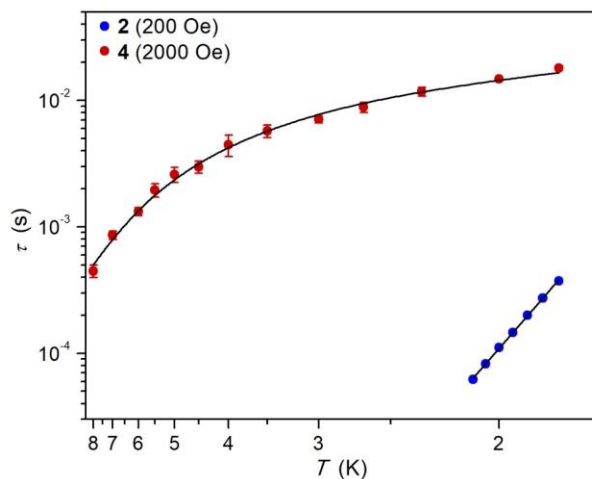
Figure 8. Arrhenius plots of relaxation time τ (log scale) versus T (inverse scale) for **2** under H_{dc} = 200 Oe (blue circles) and **4** under H_{dc} = 2000 Oe (red circles). Error bars represent the standard deviations of relaxation times. For **2**, error bars are smaller than the height of the symbols. Black solid lines represent the best fit according to the equations specified in the text. Data were collected on the 10 mM frozen solution samples in 2-MeTHF.

state separation in this compound, calculated to be between 5.1 and 5.7 cm^{-1} from the extracted D parameters.

Ac susceptibility data were also collected for **4** to examine the relaxation dynamics of the $S = \frac{1}{2}$ cluster [Cu$_4$(NP^{t}Bu$_3$)$_4$]$^+$. A microcrystalline sample of **4** showed no features of slow magnetic relaxation under zero field or applied fields, but a 10 mM frozen solution of **4** in 2-MeTHF exhibited slow magnetic relaxation as high as 8 K under an optimized field of 2000 Oe (Figure S30). The absence of zero-field relaxation in **4** is consistent with quantum tunneling of the magnetization facilitated by hyperfine interactions with the $I = \frac{3}{2}$ copper nuclear spin.[38] Since there is no magnetic excited state in an $S = \frac{1}{2}$ system, the observed slow relaxation under an applied field will arise solely due to Raman and/or direct processes according to the following equation:

$$\tau^{-1} = CT^n + AH^4T \qquad (3)$$

where C and A are coefficients for Raman and direct processes, respectively, and n is the Raman exponent. A least-squares fit to the data yielded C = 0.43(2) s^{-1}K^{-4}, n = 4, and A = 1.95(8) × 10^4 s^{-1}T^{-4}K^{-1} (Figure 8). Interestingly, the Raman relaxation times are on the order of milliseconds for **4**, similar to those previously determined for [Co$_4$(NP^{t}Bu$_3$)$_4$]$^+$ (Figure S33),[11] suggesting that the relaxation behavior may be characteristic of the spin-vibronic coupling in tetranuclear phosphinimide clusters. In the case of compound **2**, Raman relaxation on this timescale is sufficiently slow to enable exclusive observation of the Orbach barrier.

Conclusions

The foregoing results demonstrate that direct metal–metal orbital overlap in tetranuclear transition metal complexes featuring bridging tri-*tert*-butylphosphinimide gives rise to strong electronic and magnetic communication. In [Ni$_4$(NP^{t}Bu$_3$)$_4$]$^+$, a large $S = \frac{5}{2}$ ground state results from strong direct exchange via orbital overlap, while large anisotropy is engendered by the weak ligand field. Remarkably, computational results reveal

that strong ferromagnetic direct exchange in the cluster is mediated by itinerant electrons, reminiscent of magnetism in ferromagnetic metals. Intriguingly, to our knowledge, [Ni$_4$(NP^{t}Bu$_3$)$_4$]$^+$ is the first example of a single-molecule magnet with easy-plane anisotropy that exhibits slow magnetic relaxation in the absence of an applied field, as well as exclusive Orbach relaxation under a small applied field. The $S = \frac{1}{2}$ cluster [Cu$_4$(NP^{t}Bu$_3$)$_4$]$^+$ also exhibits spin-vibronic relaxation on the millisecond timescale, similar to that observed for the cobalt analogue[10] and indicative of a characteristic slow magnetic relaxation in these clusters. Finally, this study brings ferromagnetism as seen in metals into the molecular realm, presenting a new and potentially rich avenue for the design of single-molecule magnets based on metal–metal bonded clusters to achieve novel electronic, magnetic, and vibronic properties.

AUTHOR INFORMATION

Corresponding Author

* jrlong@berkeley.edu

ORCID

Khetpakorn Chakarawet: 0000-0001-5905-3578
Mihail Atanasov: 0000-0003-4178-2187
Frank Neese: 0000-0003-4691-0547
Stephen Hill: 0000-0001-6742-3620
Jeffrey R. Long: 0000-0002-5324-1321

Notes

The authors declare no competing financial interest.

REFERENCES

(1) Kahn, O. *Molecular Magnetism*; VCH, 1993.
(2) Benelli, C.; Gatteschi, D. Introduction. In *Introduction to Molecular Magnetism: From Transition Metals to Lanthanides*; Benelli, C., Gatteschi, D., Eds.; Wiley-VCH Verlag GmbH & Co. KGaA: Weinheim, Germany, 2015; pp 1–23.
(3) Gatteschi, D.; Sessoli, R.; Villain, J. *Molecular Nanomagnets*; Oxford Univ. Press, 2006.
(4) Sessoli, R.; Gatteschi, D.; Caneschi, A.; Novak, M. A. Magnetic Bistability in a Metal-Ion Cluster. *Nature* **1993**, *365*, 141–143.
(5) Milios, C. J.; Winpenny, R. E. P. Cluster-Based Single-Molecule Magnets. In *Molecular Nanomagnets and Related Phenomena*; Gao, S., Ed.; Springer Berlin Heidelberg: Berlin, Heidelberg, 2015; pp 1–109.

(6) Goddard, C. A.; Long, J. R.; Holm, R. H. Synthesis and Characterization of Four Consecutive Members of the Five-Member [Fe$_6$S$_8$(PEt$_3$)$_6$]$^{n+}$ (n = 0−4) Cluster Electron Transfer Series. *Inorg. Chem.* **1996**, *35* (15), 4347–4354.

(7) Hernández Sánchez, R.; Betley, T. A. Meta-Atom Behavior in Clusters Revealing Large Spin Ground States. *J. Am. Chem. Soc.* **2015**, *137*, 13949–13956.

(8) Hernández Sánchez, R.; Zheng, S.-L.; Betley, T. A. Ligand Field Strength Mediates Electron Delocalization in Octahedral [(HL)$_2$Fe$_6$(L′)$_m$]$^{n+}$ Clusters. *J. Am. Chem. Soc.* **2015**, *137*, 11126–11143.

(9) Hernández Sánchez, R.; Bartholomew, A. K.; Powers, T. M.; Ménard, G.; Betley, T. A. Maximizing Electron Exchange in a [Fe$_3$] Cluster. *J. Am. Chem. Soc.* **2016**, *138*, 2235–2243.

(10) Hernández Sánchez, R.; Betley, T. A. Thermally Persistent High-Spin Ground States in Octahedral Iron Clusters. *J. Am. Chem. Soc.* **2018**, *140* (48), 16792–16806.

(11) Chakarawet, K.; Bunting, P. C.; Long, J. R. Large Anisotropy Barrier in a Tetranuclear Single-Molecule Magnet Featuring Low-Coordinate Cobalt Centers. *J. Am. Chem. Soc.* **2018**, *140* (6), 2058–2061.

(12) Cook, A. W.; Bocarsly, J. D.; Lewis, R. A.; Touchton, A. J.; Morochnik, S.; Hayton, T. W. An Iron Ketimide Single-Molecule Magnet [Fe$_4$(N=CPh$_2$)$_6$] with Suppressed Through-Barrier Relaxation. *Chem. Sci.* **2020**, *68* (20), 42–61.

(13) Noodleman, L.; Case, D. A. Density-Functional Theory of Spin Polarization and Spin Coupling in Iron–Sulfur Clusters. *Adv. Inorg. Chem.* **1992**, *38*, 423–470.

(14) Bencini, A.; Ghilardi, C. A.; Midollini, S.; Orlandini, A.; Russo, U.; Uytterhoeven, M. G.; Zanchini, C. Crystal and Molecular Structure, Magnetic Properties and Scattered-Wave Description of the Electronic Structure of the Hexanuclear Octahedral Clusters [Fe$_6$(μ_3-S)$_8$(PEt$_3$)$_6$][PF$_6$]$_n$ (n = 1 or 2). *J. Chem. Soc., Dalt. Trans.* **1995**, *963* (6), 963–974.

(15) de Loth, P.; Cassoux, P.; Daudey, J. P.; Malrieu, J. P. Ab Initio Direct Calculation of the Singlet-Triplet Separation in Cupric Acetate Hydrate Dimer. *J. Am. Chem. Soc.* **1981**, *103* (14), 4007–4016.

(16) Zall, C. M.; Zherebetskyy, D.; Dzubak, A. L.; Bill, E.; Gagliardi, L.; Lu, C. C. A Combined Spectroscopic and Computational Study of a High-Spin S = 7/2 Diiron Complex with a Short Iron–Iron Bond. *Inorg. Chem.* **2012**, *51*, 728–736.

(17) Zall, C. M.; Clouston, L. J.; Young, V. G.; Ding, K.; Kim, H. J.; Zherebetskyy, D.; Chen, Y.-S.; Bill, E.; Gagliardi, L.; Lu, C. C. Mixed-Valent Dicobalt and Iron–Cobalt Complexes with High-Spin Configurations and Short Metal–Metal Bonds. *Inorg. Chem.* **2013**, *52*, 9216–9228.

(18) Kubas, A. Characterization of Charge Transfer Excited States in [2Fe–2S] Iron–Sulfur Clusters Using Conventional Configuration Interaction Techniques. *Theor. Chem. Acc.* **2020**, *139* (7), 1–7.

(19) Moriya, T. Itinerant Electron Magnetism. *Annu. Rev. Mater. Res.* **1984**, *14* (1), 1–25.

(20) Harrison, W. A. Electronic Structure and the Properties of Solids, The Physics of the Chemical Bond; Dover Publications, Inc.: New York, 1989; pp 520–529.

(21) Hay, P. J.; Thibeault, J. C.; Hoffmann, R. Orbital Interactions in Metal Dimer Complexes. *J. Am. Chem. Soc.* **1975**, *97*, 4884–4899.

(22) Willett, R. D.; Gatteschi, D.; Kahn, O. *Magneto-Structural Correlations in Exchange Coupled Systems*; Willett, R. D., Gatteschi, D., Kahn, O., Eds.; NATO ASI series: Mathematical and physical sciences; D. Reidel Pubishing Co., 1985.

(23) Anderson, P. W. Antiferromagnetism. Theory of Superexchange Interaction. *Phys. Rev.* **1950**, *79* (2), 350–356.

(24) Camacho-Bunquin, J.; Ferguson, M. J.; Stryker, J. M. Hydrocarbon-Soluble Nanocatalysts with No Bulk Phase: Coplanar, Two-Coordinate Arrays of the Base Metals. *J. Am. Chem. Soc.* **2013**, *135*, 5537–5540.

(25) Pyykkö, P.; Atsumi, M. Molecular Single-Bond Covalent Radii for Elements 1-118. *Chem. Eur. J.* **2009**, *15*, 186–197.

(26) Nicolini, A.; Galavotti, R.; Barra, A. L.; Borsari, M.; Caleffi, M.; Luo, G.; Novitchi, G.; Park, K.; Ranieri, A.; Rigamonti, L.; et al. Filling the Gap in Extended Metal Atom Chains: Ferromagnetic Interactions in a Tetrairon(II) String Supported by Oligo-α-Pyridylamido Ligands. *Inorg. Chem.* **2018**, *57* (9), 5438–5448.

(27) Barra, A. L.; Gatteschi, D.; Sessoli, R. High-Frequency EPR Spectra of a Molecular Nanomagnet: Understanding Quantum Tunneling of the Magnetization. *Phys. Rev. B - Condens. Matter Mater. Phys.* **1997**, *56* (13), 8192–8198.

(28) Biswas, R.; Ida, Y.; Baker, M. L.; Biswas, S.; Kar, P.; Nojiri, H.; Ishida, T.; Ghosh, A. A New Family of Trinuclear Nickel(II) Complexes as Single-Molecule Magnets. *Chem. - A Eur. J.* **2013**, *19* (12), 3943–3953.

(29) Layfield, R. A. Organometallic Single-Molecule Magnets. *Organometallics* **2014**, *33*, 1084–1099.

(30) Hassan, A. K.; Pardi, L. A.; Krzystek, J.; Sienkiewicz, A.; Goy, P.; Rohrer, M.; Brunel, L. C. Ultrawide Band Multifrequency High-Field EMR Technique: A Methodology for Increasing Spectroscopic Information. *J. Magn. Reson.* **2000**, *142* (2), 300–312.

(31) Malmqvist, P.-Å.; Roos, B. O. The CASSCF State Interaction Method. *Chem. Phys. Lett.* **1989**, *155* (2), 189–194.

(32) Angeli, C.; Cimiraglia, R.; Evangelisti, S.; Leininger, T.; Malrieu, J.-P. Introduction of *n*-Electron Valence States for Multireference Perturbation Theory. *J. Chem. Phys.* **2001**, *114* (23), 10252–10264.

(33) Angeli, C.; Cimiraglia, R.; Malrieu, J.-P. *N*-Electron Valence State Perturbation Theory: A Fast Implementation of the Strongly Contracted Variant. *Chem. Phys. Lett.* **2001**, *350* (3–4), 297–305.

(34) Angeli, C.; Cimiraglia, R.; Malrieu, J.-P. *n*-Electron Valence State Perturbation Theory: A Spinless Formulation and an Efficient Implementation of the Strongly Contracted and of the Partially Contracted Variants. *J. Chem. Phys.* **2002**, *117* (20), 9138–9153.

(35) Neese, F. Software Update: The ORCA Program System, Version 4.0. *WIREs Comput. Mol. Sci.* **2018**, *8* (1), e1327.

(36) Zadrozny, J. M.; Liu, J.; Piro, N. a.; Chang, C. J.; Hill, S.; Long, J. R. Slow Magnetic Relaxation in a Pseudotetrahedral Cobalt(II) Complex with Easy-Plane Anisotropy. *Chem. Commun.* **2012**, *48* (33), 3927.

(37) Frost, J. M.; Harriman, K. L. M.; Murugesu, M. The Rise of 3-d Single-Ion Magnets in Molecular Magnetism: Towards Materials from Molecules? *Chem. Sci.* **2016**, *7* (4), 2470–2491.

(38) Gómez-Coca, S.; Urtizberea, A.; Cremades, E.; Alonso, P. J.; Camón, A.; Ruiz, E.; Luis, F. Origin of Slow Magnetic Relaxation in Kramers Ions with Non-Uniaxial Anisotropy. *Nat. Commun.* **2014**, *5*, 4300.

Correlated Electrons through Metal–Metal Direct Interactions

$[Ni_4(NP^tBu_3)_4]^+$ $(S = {}^5/_2)$
$Ni_4(NP^tBu_3)_4$ $(S = 2)$

$Ni_4(NP^tBu_3)_4$

$[Ni_4(NP^tBu_3)_4]^+$